Available online at www.sciencedirect.com

ScienceDirect

Journal of the European Ceramic Society 31 (2011) 1741–1752

www.elsevier.com/locate/jeurceramsoc

Creep behaviour of porous SOFC electrodes: Measurement and application to Ni-8YSZ cermets

J. Laurencin*, G. Delette, F. Usseglio-Viretta, S. Di Iorio

CEA/LITEN, 17 rue des martyrs, F-38054 Grenoble, France

Received 8 November 2010; received in revised form 13 January 2011; accepted 23 February 2011
Available online 31 March 2011

Abstract

A methodology is proposed in this study to investigate the creep properties of porous Ni-8YSZ cermet. Creep experiments have been conducted under reducing atmosphere at the typical SOFC operating temperatures. Specimens have been loaded in a four-point bending test bench. A special attention has been paid in this work to the analytical and numerical modelling of the mechanical test. It has been highlighted that Ni-8YSZ exhibits substantial creep strain rates even at relative low temperatures ($700\,^{\circ}\mathrm{C} < T < 850\,^{\circ}\mathrm{C}$). The creep exponent has been found to be just slightly higher than unity ($1 < n < 2$) while the activation energy has been determined equal to $Q = 115\,\mathrm{kJ\,mol^{-1}}$.

High-temperature plastic strains of both Ni and 8YSZ phases have been estimated through the local stress acting on the cermet particles. This analysis indicates that creep behaviour of the Ni-8YSZ composite is not influenced by the metallic phase, but is controlled by the deformation of the 8YSZ matrix. It is also proposed that cermet creep mechanism involves Zr^{4+}cations diffusion at the surface rather than in the bulk of the 8YSZ material.

Impact of the Ni-8YSZ cermet creep on the internal stresses distribution in SOFC is discussed considering the anode supported cell (ASC) design. It is shown that cermet creep strain can induce a substantial stress decrease in the thin electrolyte.
© 2011 Elsevier Ltd. All rights reserved.

Keywords: Solid oxide fuel cell (SOFC); Cermet; Ni-8YSZ; Creep; Four-point bending test

1. Introduction

Solid oxide fuel cells (SOFCs) ensure the conversion of chemical energy into electricity at high temperature. This type of fuel cells can reach very high efficiencies compared to conventional combustion system[1–4] and represents a promising and attractive technology for power generation. However, before considering the effective deployment of such technology, the reliability of SOFCs needs to be improved. Indeed, the robustness of SOFC is still insufficient nowadays, and remains highly dependant on some operating conditions or events such as the system management failure. For instance, an accumulation of starts and shutdowns induces a degradation of the SOFC electrochemical answer which can even result in the system collapse.[5–8] These degradations have been generally ascribed to mechanical damages in the cell layers.[7,8]

Thanks to its thin electrolyte layer, anode supported cell (ASC) exhibits high electrochemical performances. Moreover, this design is especially well adapted to operate with natural gas.[9] Manufacturing process of ASC is based on a co-sintering step between the thin electrolyte and the cermet substrate.[10] This processing route generates large internal stresses in the cell due to the mismatch in thermal expansion of materials. The thin electrolyte layer is then subjected to high bi-axial compressive stresses at room temperature ($\sim -600\,\mathrm{MPa}$) which are partially reduced at $800\,^{\circ}\mathrm{C}$ upon operation.[11–13] This residual stress state tends to protect the electrolyte deposit, and delays its cracking when submitted to another tensile loading. Therefore, any electrolyte stress relaxation induced by creep deformation of the support could be detrimental regarding the ASC robustness.

The anode substrate is classically constituted by a porous cermet composed either of Nickel and 8-mol%-yttria stabilised zirconia (Ni-8YSZ) or nickel and 3-mol%-yttria stabilised zirconia (Ni-3YSZ). Both Ni and YSZ networks percolate and participate to the structural strength of the composite. Morales-Rodríguez et al.[14,15] have carried out an extensive study

---

* Corresponding author. Tel.: +33 4 38782210; fax: +33 4 38784139.
E-mail address: laurencin@chartreuse.cea.fr (J. Laurencin).

0955-2219/$ – see front matter © 2011 Elsevier Ltd. All rights reserved.
doi:10.1016/j.jeurceramsoc.2011.02.036

Nomenclature

a	spacing between the inner bearings (m)
A	pre-exponent constant of the creep power law (s^{-1} MPa^{-n})
b	specimen width (m) or Burger's vector (m)
$D_{0,l}$	frequency factor for lattice diffusion (m^2 s^{-1})
$D_{0,gb}$	frequency factor for grain boundary diffusion (m^2 s^{-1})
E	Young's modulus (MPa)
h	specimen thickness (m)
I	moment of inertia (m^4)
I_n	"complex" moment of inertia for the bending creep test ($m^{3n+1/n}$)
M_f	bending moment (N m)
n	stress exponent of the creep power law
Q	creep activation energy (kJ mol^{-1})
Q_l	lattice diffusion activation energy (kJ mol^{-1})
Q_{gb}	grain boundary activation energy (kJ mol^{-1})
s_{ij}	deviatoric part of the stress tensor (MPa)
ℓ	specimen length (m)
L	spacing between the outer bearings (m)
P	applied loading on one bearing (N)
t	time (h)
T	temperature (K)
x,y,z	system of coordinate
δ	effective boundary thickness (m)
ε_{ij}^{pl}	viscous plastic (creep) strain tensor
ε_{ij}^{elas}	elastic strain tensor
ξ	inverse of y-axis ($\xi = -y$)
ρ	beam curvature (m)
ε	porosity
ν	Poisson ratio
σ_{ij}	stress tensor (MPa)
Ω	plastic potential (MPa s^{-1}) or atomic volume (m^3)

dedicated to the creep behaviour of Ni-3YSZ cermet. By using a compressive test, they have shown that the Ni-3YSZ composite exhibits substantial creep plasticity for temperatures ranging between 900 °C and 1200 °C. In their case, it has been shown that the cermet deformation is controlled by the 3YSZ ceramic backbone. Few studies have been devoted to the Ni-8YSZ composite. Gutierrez-Mora et al.[16] have deformed in compression anode-supported bilayers at strain rates ranging between 10^{-5} and 5×10^{-4} s^{-1}. Their results suggest that creep of Ni-8YSZ can arise above 1000 °C. Other authors suspect that creep could even occur at the SOFC operation temperature: Sarantaridis et al.[17] suggest that the plastic deformation of 8YSZ ceramic network could accommodate the increase in solid volume when the Ni phase is oxidised into NiO at 800 °C. This hypothesis of a plastic deformation of 8YSZ phase in SOFC cermet is consistent with the creep observed in plasma–sprayed thermal barrier coatings. Indeed, several authors have highlighted[18–21] a substantial creep strain for 8YSZ plasma coatings tested at low temperatures (800 °C) and low stress levels (20–50 MPa). These results reinforce the claim that the Ni-8YSZ could creep in the SOFC operation conditions; even if microstructures between SOFC cermet and plasma sprayed coatings are rather different.

This article is dedicated to the study of viscoplastic deformation of Ni-8YSZ cermet at intermediate temperature. The creep behaviour has been investigated in the SOFC operating temperatures and for loadings which correspond to the internal stresses in anode due to the cell manufacturing process (~20 MPa at 800 °C).[13] A creep mechanism has been proposed for the studied conditions, through the local stress acting on each phase of the composite. Finally, the impact of the measured creep strain rates on stress relaxation in SOFCs has been also assessed for the ASC design.

Creep measurements were conducted using four-point bending test.[22] It can be noticed that the flexural test does not require specific machining and clamping, and thus, it allows overcoming several drawbacks encountered with other mechanical tests. Furthermore, the bending test is especially well adapted to the geometry of SOFC electrodes or electrolyte membranes.[23] However, it is worth underlining that some difficulties arise in the bending creep test.[24] Conversely to the uniaxial creep tensile test, the stress is non homogeneous and, furthermore, its distribution in the beam evolves with time. As a consequence, it is not straightforward to obtain a relationship between the strain rate and the applied loading. In the frame of this article, a semi-analytical formulation has been proposed in order to exploit the experimental creep curves assuming a stabilised regime. This domain is reached after a time which depends non-explicitly on the studied creep material parameters. Thus, once those parameters are identified, it is necessary to check the validity of the semi-analytical formulation by a Finite Element (FE) analysis. All this points constitutes a methodology which is presented in the article.

2. Experimental procedure

2.1. Material and samples preparation

Experiments have been conducted using commercial SOFC anode supports[10] supplied by the Forschungszentrum Jülich (FZJ) research centre. As received, the material is constituted of 56 wt.% NiO and 44 wt.% 8YSZ (ZrO_2 stabilized with 8 mol% Y_2O_3). Rectangular specimens with nominal dimensions of 7 mm × 40 mm and 1 mm thick were prepared by laser cutting (Fig. 1). It can be noticed that edges of the samples were slightly polished to remove the zone thermally affected by the preparation.

Before testing, specimens were heated up to $T = 800$ °C at a rate of 5 °C min^{-1} under (2%H_2 + Ar). They were maintained at these temperature and atmosphere conditions during 48 hours in order to achieve the complete reduction of NiO into Ni. This procedure has been qualified by RX diffraction spectra indicating that all the Ni species are present under metallic form after the reduction treatment. Cermet open porosity was determined by Archimedes' method and is equal to ~27% in the fully oxidised state and ~43% in the reduced state.

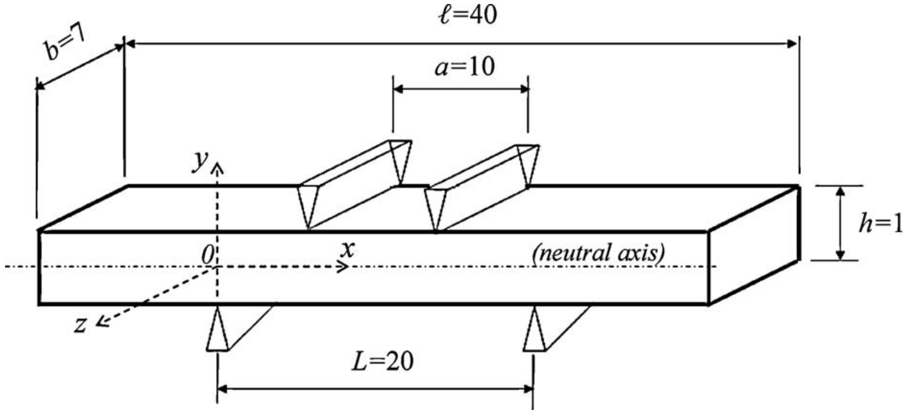

Fig. 1. Geometry of the four-point bending test and system of coordinated used for the modelling (dimensions are given in mm).

2.2. Description of the flexural creep testing

Specimens were loaded in a four-point bending setup. The spacing of the outer bearings was fixed to $L = 20$ mm whereas the span between the inner ones was adjusted to $a = 10$ mm (Fig. 1). Creep tests were carried out within the temperature range of 700–850 °C. The furnace was heated at 5 °C min^{-1} up to the testing temperature, and its chamber was swept under (2%H_2 + Ar) flux in order to preserve the cermet in its Ni-8YSZ reduced state.

Specimens were loaded at a high rate until to reach the targeted stress for creep experiments. During this initial loading, the beam deflection was controlled to 300 μm min^{-1}. It has been checked that, under this condition, the behaviour of the specimen remains purely linear and reversible during the initial loading. Creep experiments were then conducted by applying a constant load *2P*, corresponding to an initial maximum stress in the outer fibre of the specimen ranging between 8.5 and 23.0 MPa. Note that these stress levels are evaluated by the linear beam theory, and are expressed by the following expression[25]:

$$\sigma_x^{\max} = \frac{hM_f}{2I} \quad \text{with} \quad I = \frac{bh^3}{12} \text{ and } M_f = P\frac{L-a}{2} \tag{1}$$

where M_f is the bending moment and I is the moment of inertia, which depends on the beam width b and thickness h.

The applied load $2P$ was controlled with a high resolution force transducer (±0.1 N). Specimen deflection was measured during the creep test. For this purpose, the displacement of the central point of the beam was recorded by using a high-temperature extensometer with a resolution of ±0.5 μm. The extensometer consisted in an alumina rod associated to an LVDT sensor placed in a cooled zone of the furnace. The extensometer was designed in such way that its stiffness was much lower than the tested specimen.

It is worth noting that all the creep experiments have been performed under reducing atmosphere. Indeed, this condition is representative of SOFC operation. Moreover, it has to be keeping in mind that the oxidised NiO-YSZ cermet presents a purely elastic behaviour in the conditions investigated in this work (*i.e.* at $T = 800$ °C and low stresses). This claim has been checked in the present study: as expected, it has been found that no creep strain has been recorded at 800 °C under an oxidizing condition (air) when the cermet is submitted to an applied load of $2P = 9.3$ N ($\sigma_x^{\max} = 20$ MPa).

3. Basic relations for the creep parameters identification

3.1. Analytical formulation in the stabilised regime

An analytical formulation is proposed here to determine the creep parameters from the experiments. Hollenberg et al.[22] have initially proposed a 2D analytical calculation of the four-point bending creep test assuming the plane stress condition. Based on this initial approach, the modelling has been generalised here to the plane strain hypothesis. A detailed description of the analysis is provided in Appendix A. The main hypothesis are summarised here after. The primary creep is neglected and the material behaviour is considered to be identical in compression and in traction. For the stationary creep regime, the inelastic strain rate $d\varepsilon^{pl}/dt$ is supposed to follow the classical power law (or Norton's) model:

$$\frac{d\varepsilon^{pl}}{dt} = A \times \sigma^n \quad \text{with} \quad A = B \times e^{-Q/RT} \tag{2}$$

where T is the temperature, Q the apparent activation energy for creep and n the stress exponent. The term ε^{pl} denotes the creep strain whereas σ corresponds to the applied stress for a homogeneous and uni-axial loading. The pre-exponential constant B depends on the material microstructure.

When applied for the bending creep test, the power law model leads to the following expression for the stress component σ_x calculated at a distance ξ of the neutral axis (with $\xi = -y$: see system of coordinate in Fig. 1):

$$\sigma_x(\xi) = \frac{\xi^{1/n} \times M_f}{I_n} \quad \text{with} \quad I_n = 2b \times \frac{n}{n+1} \times \left(\frac{h}{2}\right)^{(2n+1)/n} \tag{3}$$

where I_n is defined as the "complex" moment of inertia, which depends in this case on the beam dimensions (*i.e.* beam width b and thickness h) but also on the stress exponent n. Relation (3) stands for describing the stress profile for both the plane stress analysis and the plane strain approximation. This relation has been stated assuming that the elastic strain is constant (see Appendix A). As a consequence, Eq. (3) corresponds to the stationary solution of the flexural creep problem, and then, is fulfilled after a sufficient duration of creep test:

For $n = 1$, it can be noticed that Eq. (3) reduces to a linear stress profile identical to the result established in elasticity. However, for n higher than unity, the stress profile along the beam thickness becomes non linear. As a consequence, a transient evolution appears from the initial linear stress profile, which is obtained at short times where elastic strains are dominant, to the non-linear profile established for long times. This transition always occurs in flexural creep test (for $n > 1$) even if the condition of a "secondary creep" regime (characterised by the power law creep) is fulfilled. The materials parameter of Norton's law has to be identified considering only data obtained after this transition has occurred. This point will be checked in the Section 4.3 by using the creep data obtained in Section 4.1.

For the stationary regime, it is demonstrated in Appendix A that the shape of the deflected beam depends of the applied loading $2P$ according to the following equations:

$$y(x) = -J(t) \times \left(\frac{P}{I_n}\right)^n \times \Gamma(x) \quad \text{for} \quad x \in \left[\frac{L-a}{2}; \frac{L+a}{2}\right] \tag{4a}$$

$$y(x) = -J(t) \times \left(\frac{P}{I_n}\right)^n \times \Lambda(x) \quad \text{for} \quad x \in \left[0; \frac{L-a}{2}\right] \cup \left[\frac{L+a}{2}; L\right] \tag{4b}$$

where the Γ and Λ functions depend on the stress exponent n and the spacing between the inner and outer bearings a and L. Their expressions are given in Appendix A. The term $J(t)$ contains the time-dependence on strain and is expressed from the power law creep model:

$$J(t) = A \times t + \text{constant} \quad \text{For plane stress} \tag{5a}$$

$$J(t) = A \times \left(\frac{3}{4}\right)^{(n+1)/2} \times t + \text{constant} \quad \text{For plane strain} \tag{5b}$$

Plotting in logarithmic scale the beam deflection rate, $\left.\frac{\partial y}{\partial t}\right)_{x=L/2}$, versus the applied loading on one bearing P allows determining the creep parameters n and A. It can be noticed that a substantial difference can arise for the determination of A whether the plane stress or plane strain conditions are considered for the experimental results analysis. According to the tested specimen geometry, the real stress state ranges between these two conditions. Therefore, it is proposed to weight the pre-exponent constant A according to the following mixture law:

$$A = \omega \times A^{plane\ strain} + (1 - \omega) \times A^{plane\ stress} \tag{6}$$

$A^{plane\ stress}$ corresponds to the pre-exponent constant obtained by fitting the experimental data by using Eqs. (4) and (5a) in plane stress condition, whereas $A^{plane\ strain}$ is obtained by using Eqs. (4) and (5b) considering the plane strain assumption.

3.2. Determination of the weighting parameter ω

A 3D finite element analysis of the creep test has been carried out in order to determine which approximation (plane stress or plane stain analysis) is more suited for the exploitation of the flexural test. The material data used for the computation are summarised in Table 1. The reported value for Young's modulus has been measured in the present study by recording the elastic slope during the initial specimen loading. It can be noticed that this value is also consistent with the Young's modulus obtained on the FZJ Ni-8YSZ cermet by using a four-point bending test bench.[27]

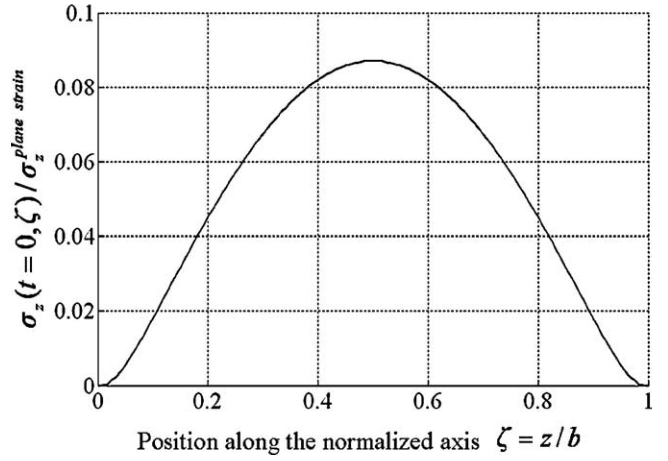

Fig. 2. The term $f(\zeta) = \sigma_z(t,\zeta)/\sigma_z^{plane\ strain}$ is plotted along the normalized axis $\zeta = z/b$ along the beam width. f is calculated at $t = 0$ and for $x = L/2$ and $y = -h/2$ (see system of coordinate in Fig. 1, Applied loading $2P = 7N$ ($\sigma_x^{\max,t=0} = 15$ MPa)).

An adimensional parameter f has been defined to quantify the local beam stress state.

$$f(\zeta) = \frac{\sigma_z(t,\zeta)}{\sigma_z^{plane\ strain}} \text{ with } \zeta = \frac{z}{b} \tag{7}$$

f is defined as the ratio of the simulated stress σ_z to the bound value $\sigma_z^{plane\ strain}$ which is given analytically by the plane strain condition. At $t = 0$, the term $\sigma_z^{plane\ strain}$ is equal to the value obtained in elasticity ($= \nu\sigma_x$). For $t > 0$, $\sigma_z^{plane\ strain}$ tends to $\sigma_x/2$ (see detail in Appendix A).

Along an axis parallel to the beam width, the parameter f increases from the plane stress value on the beam edge ($f = 0$), and tends to the plane strain value on the beam centre ($f = 1$). A typical evolution of f along the beam width is illustrated at $t = 0$ in Fig. 2.

This ratio f is integrated along the normalised beam width to obtain a mean value:

$$\bar{f} = \int_{\zeta=0}^{\zeta=1} \frac{\sigma_z(t,\zeta)}{\sigma_z^{plane\ strain}}\, d\zeta \text{ with } \zeta = \frac{z}{b}\ (at\ x = L/2\ and\ y = -h/2) \tag{8}$$

It is found that $\bar{f}$ increases slowly from 5.1% in case of pure elasticity (at $t = 0$) to an asymptotic value equal to 7.3% for the steady-state creep (at $t = 200$ h). This result implies that only a small volume of the specimen is submitted to the plane strain condition, the other part being loaded in a state close to the plane stress condition. From this result, it has been proposed to take $\omega = 0.073$.

Table 1
Data used for the simulations.

	Elastic parameters		Constant of the creep power law[a]	
	Young's modulus at 800 °C E (GPa)	Poisson ratio ν	Stress exponent n	Pre-exponent constant A (s^{-1} MPa^{-n})
Ni-8YSZ cermet (reduced state)	29 [27]	0.29 [28]	1.7	2.64×10^{-11}

[a] Data obtained in the present study.

4. Experimental results and data analysis

4.1. Creep curves: identification of the pre-exponent constant A and stress exponent n

Typical evolution of the beam deflection $\Delta y_{x=L/2}$ obtained during the creep experiments is illustrated in Fig. 3 at 800 °C. Specimens exhibit substantial deformations even for low applied loadings. A transient regime is clearly observed for times lower than 20 h and could be reasonability ascribed to the primary creep domain. This regime is followed by an inelastic flow characterised by a nearly constant slope in the experimental curve. It corresponds to the steady-state or “secondary creep” domain. It is worth underlying that these experimental results prove that non negligible creep deformation of Ni-YSZ cermet arise in SOFC operating condition: the beam deflection after 100 h is two times higher than the value obtained for an elastic behaviour.

Experimental raw creep curves need to be processed before identifying both A and n parameters of the Norton's law. For this purpose, time-derivation of the experimental curves has been performed numerically to compute the beam deflection rate. Steady-state creep rates have been considered to be achieved for time extending beyond $t = 35$ h. This threshold allows avoiding the primary creep regime. It will be checked in Section 4.3 that this time is also sufficient to ensure that stresses are quasi-stabilised allowing that relations (3), (4) and (5) are fullfilled.

Fig. 4a and b shows the stationary beam deflection rates $\left.\frac{\partial y}{\partial t}\right)_{x=L/2,\,t\geq 35\,\mathrm{h}}$ versus the applied loadings P plotted in logarithmic coordinates at 800 °C and 750 °C. The experimental data have been fitted by a linear regression in order to identify the creep parameters according to the procedure presented in the previous modelling section. Creep effective pre-exponent A and stress exponent n are tabulated for both 750 °C and 800 °C temperatures (Table 2). It can be noticed that stress exponents determined here are just slightly higher than unity ($n = 1.1$–1.7). This result indicates that creep of Ni-YSZ cermet is consistent with a mechanism involving a diffusional process.[29]

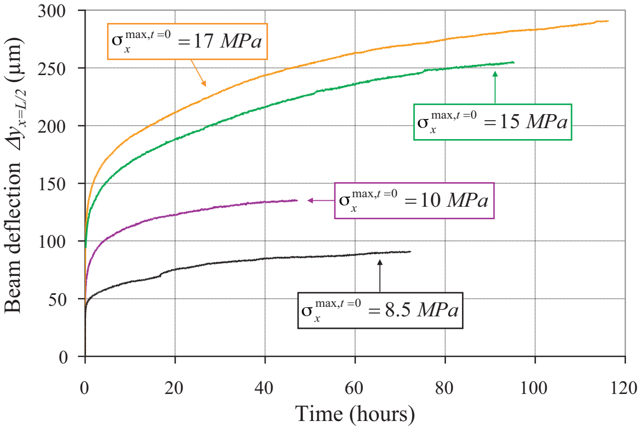

Fig. 3. Illustration of beam deflections plotted as a function of time. The deflections have been recorded during the bend creep test under a range of stresses at 800 °C.

4.2. Effect of temperature: identification of activation energy Q

Creep curves were measured for temperatures ranging from 700 °C to 850 °C on specimens submitted to an applied load of $2P = 8N$ ($\sigma_x^{\max,\,t=0} = 17$ MPa) (Fig. 5). It can be noticed that the sample tested at 850 °C has broken for a creep time of ~95 h.

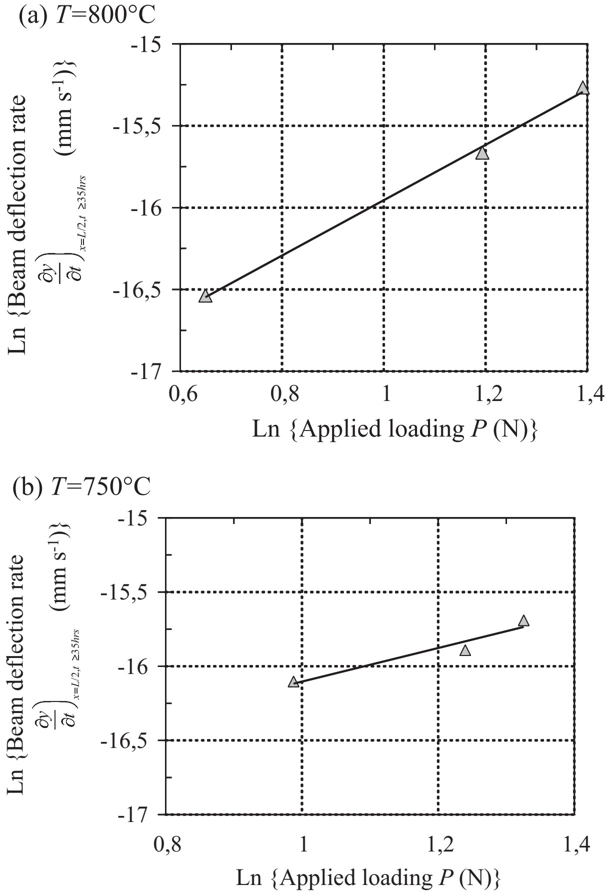

Fig. 4. Stationary beam deflection rate $\left.\frac{\partial y}{\partial t}\right)_{x=L/2,t\geq 35\ \mathrm{h}}$ plotted as a function of the applied loading on one bearing P in logarithmic coordinate at 800 °C. The solid line corresponds to the least-squares fit to experimental data: $T = 800$ °C; $T = 750$ °C.

Table 2
Creep parameters of the power law model determined by four-point bending test on Ni-YSZ cermet (reduced state).

Temperature	Pre-exponent A (s^{-1} MPa^{-n})	Stress exponent n	Activation energy Q (kJ mol^{-1})
$T = 750\,°C$	7.2×10^{-11}	1.1	–
$T = 800\,°C$	2.6×10^{-11}	1.7	–
$700\,°C \leq T \leq 850\,°C$	–	–	115

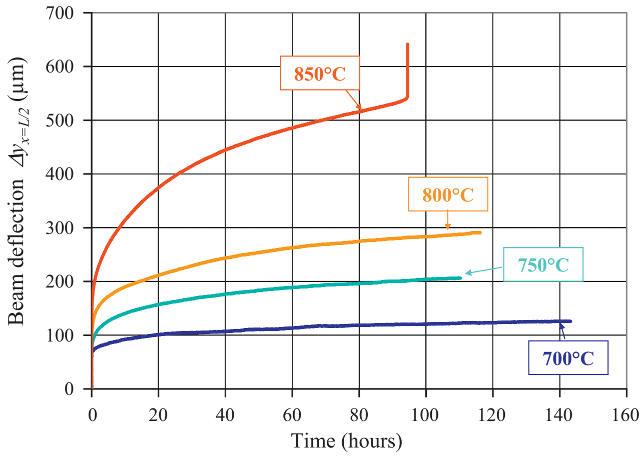

Fig. 5. Effect of temperature on creep behaviour of Ni-YSZ cermet. The creep data have been measured for temperature ranging from 700 °C to 850 °C under an applied loading $2P = 8N$ ($\sigma_x^{\max,\, t=0} = 17$ MPa).

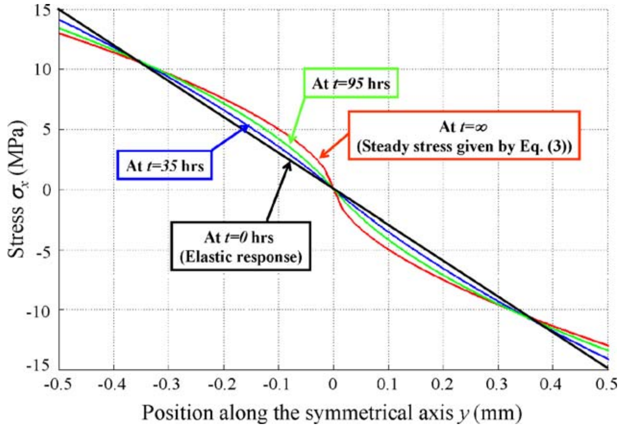

Fig. 7. Simulated stress $\sigma_x(t)$ plotted along the symmetrical axis of the beam ($x = L/2$, plane stress). The profiles depend on time and are compared to the stabilised stress at $t = \infty$ given by Eq. (3). (Applied loading $2P = 7N(\sigma_x^{\max,t=0} = 15$ MPa)).

However, this time remains sufficient to identify a stabilised value of the beam deflection rate. As represented in Fig. 6, the stationary beam deflection rates $\left.\frac{\partial y}{\partial t}\right)_{x=L/2,t\geq 35\,\mathrm{h}}$ are plotted in logarithmic coordinate as a function of the inverse temperature $1/T$. In this Arrhenius-type plot, the experimental data exhibit a linear behaviour. The slope obtained from a linear fit provides according to Eq. (2) the activation energy for creep deformation. The value of $Q = 115$ kJ mol^{-1} is obtained.

4.3. Determination of time for the stress stabilisation

As mentioned in Section 4.1, the time required for stress stabilisation can now be evaluated considering the identified creep parameters. Simulations have been performed to assess this time necessary to reach the stress steady-state. The numerical analysis has been restricted to a 2D simulation assuming the plane stress state for the (x 0 y) cross section of the beam (*i.e.* $\sigma_z = 0$).

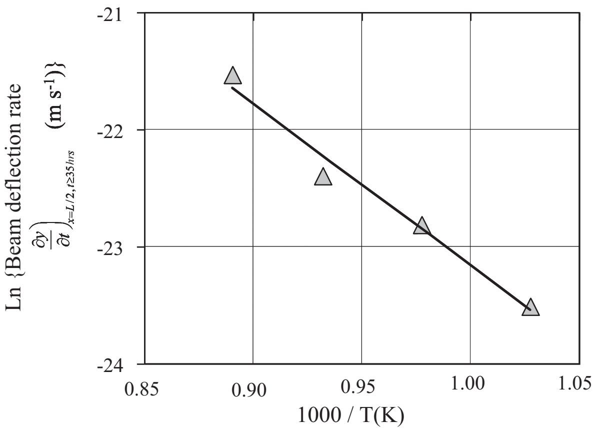

Fig. 6. Stationary beam deflection rate $\left.\frac{\partial y}{\partial t}\right)_{x=L/2,t\geq 35\ \mathrm{h}}$ versus the inverse of temperature $1000/T$ in logarithmic coordinate.

Fig. 7 shows the evolution with time of the $\sigma_x(t)$ stress component plotted along the symmetrical axis of the beam (*i.e.* for $x = L/2$). Profiles range from the elastic solution at $t = 0$ to the plastic one corresponding to the steady-state described by Eq. (3) at $t = \infty$. It can be noticed that the difference between the two bounded solutions at $t = 0$ and $t = \infty$ are slight, meaning that the mechanical response of the specimen is not strongly impacted by the stress redistribution during the creep test.

In order to quantify the degree of stress stabilisation, a parameter $\wp(t)$ has been defined as followed:

$$\wp(t) = \left(\frac{A_{t=\infty} - A_t}{A_{t=\infty}}\right) \quad \text{with } A_t = \int_{y=0}^{y=-h/2} \sigma_x(t)dy\,(x = L/2) \tag{9}$$

where $A_{t=\infty}$ corresponds to the steady stress integrated along the beam height:

$$A_{t=\infty} = \int_{\xi=0}^{\xi=h/2} \frac{\xi^{1/n} \times M_f}{I_n} d\xi = \frac{n}{n+1}\frac{M_f}{I_n}\left(\frac{h}{2}\right)^{(1+n)/n}$$
$$(x = L/2, \quad \xi = -y) \tag{10}$$

The parameter $\wp(t)$ is plotted as a function of time in Fig. 8: it decreases during the test and tends to *0* when the steady state is fully reached. This evolution allows determining a criterion on stress stabilisation defined for $\wp(t) \leq 10\,\%$. This criterion leads to identify the creep parameters on the experimental measurements only for time $t > 34$ h, as assumed in Section 4.1.

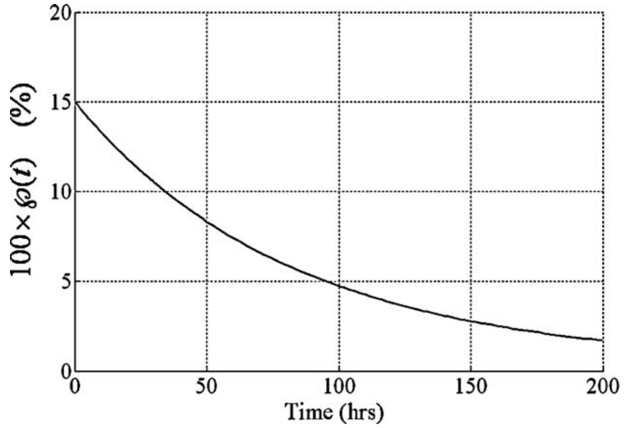

Fig. 8. The parameter $\wp(t)$ is plotted as a function of time. Expression of $\wp(t)$ is provided by Eqs. (9) and (10). $\wp(t)$ is calculated with stress profiles of Fig. 7.

5. Discussion

5.1. *Mechanism of Ni-YSZ creep deformation*

5.1.1. *Phase controlling the cermet creep strain*

The studied cermet is composed by both Ni and 8YSZ phases which are entangled together. The metallic component percolates since the composite is a good electric conductor. It has been also checked in the present study that the ceramic particles are sintered into a percolating network: the Ni component has been removed from the composite by its dissolution into HNO_3. The strength of the obtained highly porous ceramic backbone (as shown in Fig. 9) has been assessed to ∼5 MPa at $T = 800\,°C$ in a flexural test rig. This result means that 8YSZ particles are connected to each other and constitute a mechanically stable network. As a consequence, the creep deformation of the Ni-YSZ composite is liable to be controlled either by the ceramic or metallic phases or both.

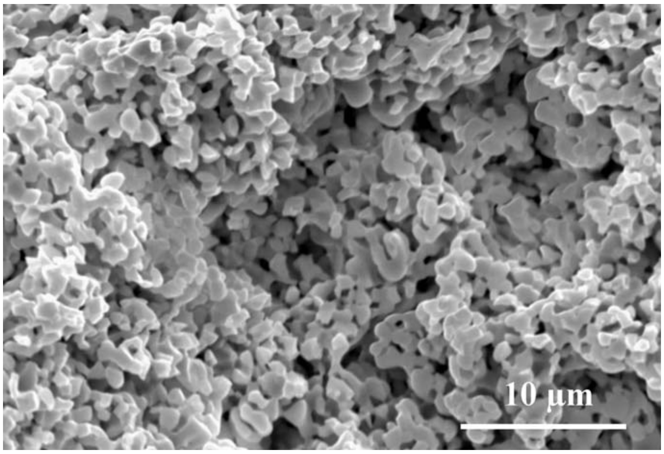

Fig. 9. Surface of 8YSZ network examined with a scanning electron microscope (SEM) after dissolution of the Ni phase in the Ni-8YSZ cermet. The complete Ni dissolution into HNO_3 has been checked by weight measurements before and after the acid attack.

Scanning electron microscope (SEM) examinations of specimen have been carried out after the creep test. The observations have revealed the absence of internal cracks into the cermet. As a consequence, inelastic deformations in each phase are involved in the resulting macroscopic strain of the composite.

In order to estimate the Ni and 8YSZ creep strain rates, the local stress σ_{local} acting on the solid backbone has to be determined. This stress level can be estimated from the macroscopic stress σ_{appl} applied on the cermet according to a simple geometrical model[15,30]:

$$\sigma_{local} = \frac{\sigma_{appl}}{1-(\pi/4)(6\varepsilon/\pi)^{2/3}} \tag{11}$$

where ε denotes the cermet porosity. Then, from this resulting stress supposed to act identically on both Ni and YSZ networks, an estimation of the creep deformation of each phase is proposed by using creep laws relevant for each material (Ni and YSZ):

In the condition of this study, Ni creep mechanism is based on diffusional flow of vacancies.[31] Vacancies can diffuse either through the bulk of crystallographic grains (Nabarro–Herring creep) or along the grains boundaries (Coble creep). Both mechanisms are thermally activated mechanism and are combined into the following expression[32,33,34] which provides the uni-axial creep strain rate $d\varepsilon_{Ni}^{pl}/dt$:

$$\frac{d\varepsilon_{Ni}^{pl}}{dt} = 14\frac{D_l^{Ni}\sigma_{local}\Omega_{Ni}}{kTd_{Ni}{}^2}\left[1+\frac{\pi\delta_{Ni}}{d_{Ni}}\frac{D_{gb}^{Ni}}{D_l^{Ni}}\right] \tag{12}$$

where k denotes the Boltzmann's constant, Ω_{Ni} the atomic volume, d_{Ni} the grain size and δ_{Ni} the effective grain boundary thickness. D_{gb}^{Ni} and D_l^{Ni} correspond to the diffusion coefficients respectively along the grain boundaries (Coble creep) or through the grain lattice (Nabarro–Herring creep). The diffusion coefficients depend on the temperature according to an Arrhenius law[32,34]:

$$D_l^{Ni} = D_{0,l}^{Ni}\times\exp\left(-\frac{Q_l^{Ni}}{RT}\right) \quad \text{and} \quad D_{gb}^{Ni} = D_{0,gb}^{Ni} \times\exp\left(-\frac{Q_{gb}^{Ni}}{RT}\right) \tag{13}$$

where D_0 and Q are respectively a frequency factor and activation energy for the appropriate diffusion process.

In the range of the considered operating conditions, creep of 8YSZ is controlled by the migration of Zr^{4+} cations which are to the slower diffusing specie in the compound.[35–38] The uni-axial high-temperature plastic strain rate $d\varepsilon_{8YSZ}^{pl}/dt$ is a combination of Coble and Nabarro–Herring creep processes[39]:

$$\frac{d\varepsilon_{8YSZ}^{pl}}{dt} = 9.3\frac{D_l^{8YSZ}\sigma_{local}b^3}{kTd_{8YSZ}{}^2}\left[1+3.6\frac{\delta_{8YSZ}}{d_{8YSZ}}\frac{D_{gb}^{8YSZ}}{D_l^{8YSZ}}\right] \tag{14}$$

where b denotes the Burgers vector. The temperature dependence of lattice and grain boundaries diffusion coefficients D_l^{8YSZ} and D_{gb}^{8YSZ} are also expressed according to an Arrhenius

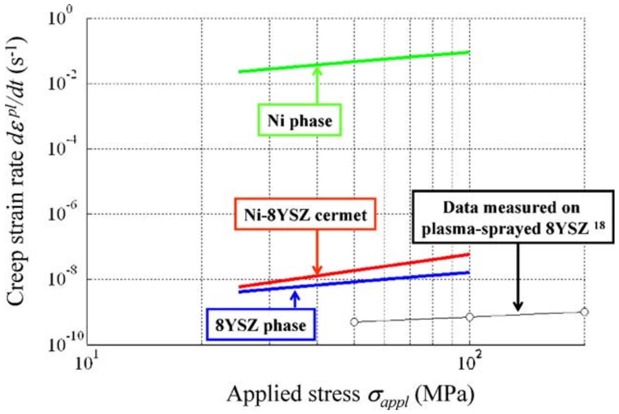

Fig. 10. Plot of creep strain rate versus the applied stress at 800 °C for Ni-8YSZ cermet, Ni and 8YSZ phases of the composite studied here. Data measured for 8YSZ plasma-sprayed coating at 800 °C under air are added for comparison.[18]

law[36]:

$$D_l^{8YSZ} = D_{0,l}^{8YSZ} \times \exp\left(-\frac{Q_l^{8YSZ}}{RT}\right) \quad \text{and} \quad D_{gb}^{8YSZ} = D_{0,gb}^{8YSZ} \times \exp\left(-\frac{Q_{gb}^{8YSZ}}{RT}\right) \tag{15}$$

In Fig. 10, several creep strain rates have been plotted as a function of the applied stress σ_{appl} by considering an uni-axial tensile test at 800 °C. The deformation of Ni and 8YSZ phases have been calculated considering the set of Eqs. (11)–(15). Parameters values required for the numerical analysis are listed in Table 3. The Ni-YSZ cermet curve has been added by using the creep parameters measured in the present study (see Table 2).

As shown in Fig. 10, deformation of Ni phase is found to be much higher than the cermet one. This result indicates than Ni phase does not limit the deformation of the composite. Conversely, creep strain rate of 8YSZ phase is found to be in the same order than as the cermet one. This last result means that the ceramic matrix controls the creep behaviour of the Ni-8YSZ cermet.

Data measured on 8YSZ plasma-sprayed coating at 800 °C[18] have been added in Fig. 10. The creep rate is found to be roughly in the same range than the one obtained for the present cermet. As a consequence, this comparison reinforces the claim that creep deformation of the cermet is controlled by the 8YSZ material. However, a slight discrepancy in creep behaviour can be noticed between the cermet and the 8YSZ plasma-sprayed coating. This could be explained by the difference in microstructures (induced by different manufacturing methods). For instance, porosity of the plasma-sprayed coatings (∼10%) is substantially lower than the cermet one (∼43%).

5.1.2. Mechanism of porous 8YSZ creep

As shown in Fig. 10, the creep rate of the cermet is found to be slightly higher than the calculated deformation of 8YSZ matrix. This "accelerated" creep rate could be explained by the experimental reducing atmosphere required to keep the cermet in its reduced state (and which is representative of SOFC operation). Indeed, as shown by Zhu et al.[18], this condition tends to increase the creep rates of porous 8YSZ. The authors have proposed to ascribe this phenomenon to an enhancement of the metal cation interstitial diffusion.

Ni-8YSZ creep activation energy measured in this work (=115 kJ mol^{-1}) is found to be substantially lower than monolithic 8YSZ activation energy for both Nabarro–Herring ($Q_l^{8YSZ} = 460$ or 440 kJ mol^{-1} [36,40]) and Coble creep processes ($Q_{gb}^{8YSZ} = 309$ kJ mol^{-1} [36]). Conversely, Ni-8YSZ cermet creep activation energy is found to match with the values measured on porous 8YSZ and 7YSZ plasma-sprayed coatings: $Q_{plasma}^{8YSZ} = 104$ or 190 kJ mol^{-1} [19,20], $Q_{plasma}^{7YSZ} = 134$ or 114 kJ mol^{-1} [41,42]. It is worth underlining that these last reported values for plasma coatings have been measured in the same temperature range than the one considered in the present study (800 °C < T < 1100 °C). Zhu et al.[19] and Withney et al.[41] have proposed an explanation to this low activation energy: creep deformation of porous 8YSZ plasma-sprayed coatings at T < 1100 °C could be controlled by a Zr^{4+} surface diffusion, while bulk diffusion would be dominant for higher temperatures. This suggestion can be reasonably extended to the creep deformation of ceramic phase into the cermet. Indeed, as already mentioned, both plasma coating and cermet materials present similar creep activation energy. Moreover, this conclusion is consistent with the study carried out by Erk et al.[43] on 7YSZ. These authors have shown that surface diffusion is the dominant mass transport mechanism in YSZ at relatively low temperature ($T \leq 1000$ °C), whereas Zr^{4+} volume diffusion become active for higher temperatures ($T \geq 1200$ °C).

5.2. Impact of creep behaviour on SOFC internal stresses

It has been shown in the present study that Ni-8YSZ composite can exhibit a substantially creep deformation as soon as the temperature reaches 700 °C. This high-temperature plastic behaviour could have a strong influence on the SOFC mechanical robustness.

5.2.1. ASC configuration

In the case of ASC design, cell manufacturing induces internal stress within the cell layers. The thin electrolyte is subjected to a high compressive bi-axial stress which is balanced by a tensile component in the Ni-8YSZ substrate.[12,13] Relaxation of the cell internal stresses could occur in operation since the Ni-8YSZ creep strain is likely to arise at the SOFC operating temperature. In order to estimate this risk, finite element computations have been carried out at 800 °C considering a circular half cell (constituted by a thick Ni-8YSZ anode associated with a thin and dense electrolyte of 8YSZ: see cell dimensions in Table 4). Stress calculation can be divided according to the three following steps:

(i) *Manufacturing stresses*[13]: Internal stresses are computed after the cell cooling from the sintering temperature (T = 1350 °C) down to operating temperature (T = 800 °C).

Table 3
Coble and Nabarro–Herring creep parameters for monolithic Ni and 8YSZ materials.

	Frequency factor for lattice diffusion $D_{0,1}$ ($m^2\ s^{-1}$)	Activation energy for lattice diffusion Q_1 ($kJ\ mol^{-1}$)	Atomic volume Ω (m^3)	Burger's vector b (m)
Nickel	1.9×10^{-4} [34]	284 [34]	1.09×10^{-29} [34]	–
8YSZ	2.2×10^{-5} [36]	460 [36]	–	2.57×10^{-10} [39]
	Frequency factor for GB diffusion $D_{0,gb}$ ($m^2\ s^{-1}$)	Activation energy for GB diffusion Q_{gb} ($kJ\ mol^{-1}$)	Effective boundary thickness δ (m)	Grain size d (m)
Nickel	5.0×10^{-6} [34]	115 [34]	7.0×10^{-10} [44]	1.0×10^{-6} [a]
8YSZ	1.5×10^{-3} [36]	309 [36]	1.0×10^{-9} [36]	1.0×10^{-6} [a]

[a] Typical value for SOFC Ni-YSZ composite[31].

Table 4
Geometry and elastic parameters of the simulated half cell.

	Half cell geometry		Elastic parameters		
	Diameter (mm)	Layer thickness (μm)	Young's modulus E (MPa)	Poisson ratio ν	TEC[a] (K^{-1})
Oxidised anode (NiO-8YSZ)	25	1000	68 [27]	0.29 [28]	12.5 [b]
Reduced anode (Ni-8YSZ)	25	1000	29 [27]	0.29 [28]	12.5 [28]
Electrolyte (8YSZ)	25	10	216 [28]	0.311 [28]	10.8 [45]

[a] Thermal expansion coefficient.
[b] Assumed to be equivalent to Ni-8YSZ.

Stresses arise because of the mismatch in thermal expansion coefficients (TECs) between cell layers. The cermet has to be considered in its oxidised state during this manufacturing step. Therefore, simulations have been performed considering a purely elastic behaviour for each cell layer (it is reminded that no creep has been recorded in the present study when the cermet is in its NiO-YSZ oxidised state).

(ii) *Stresses after reduction*[13]: The second step is devoted to the cermet reduction under an H_2 atmosphere. Stresses modification is assumed to be induced by the decrease of cermet Young's modulus (Table 4).

(iii) Stress relaxation by cermet creep strain: Stress evolution in time due to the cermet creep at the SOFC operating temperature has been computed by implementing the power law model in the software (with the parameters values given in Table 2).

A detailed description of the methodology to simulate cell stresses after manufacturing and cermet reduction can be found in Ref.[13] Simulations have been carried out with the elastic parameters provided in Table 4. Fig. 11 shows the modifications of the electrolyte bi-axial stress taken in the middle of the cell. Since reduction of anode leads to a very slight decrease in the stress level ($\Delta\sigma_{bi\text{-}axial} = 35$ MPa), electrolyte remains submitted to a favourable high compression after the treatment. It can be noticed that this simulated result is in good agreement with stress measurements carried out by Fischer et al.[11] on the same kind of cell. However, as illustrated in Fig. 11, cermet creep strain could involve a high stress decrease into the electrolyte. For instance, it is found that the electrolyte compression is two times lower after an operating duration of ~500 h at $T = 800$ °C. This significant electrolyte stress relaxation could be detrimental regarding to its robustness. Cell 'redox' tolerance will be especially reduced since cermet re-oxidation induces a high tensile component in the thin electrolyte.[7]

5.2.2. *ESC configuration*

In the case of electrolyte supported cell (ESC) design, the Ni re-oxidation under an air stream induces a bulk cermet expansion which leads to a very high compressive stress in the thin cermet layer.[13] This stress level is only partially decreased after a second reduction under a hydrogen flow. Therefore, the cer-

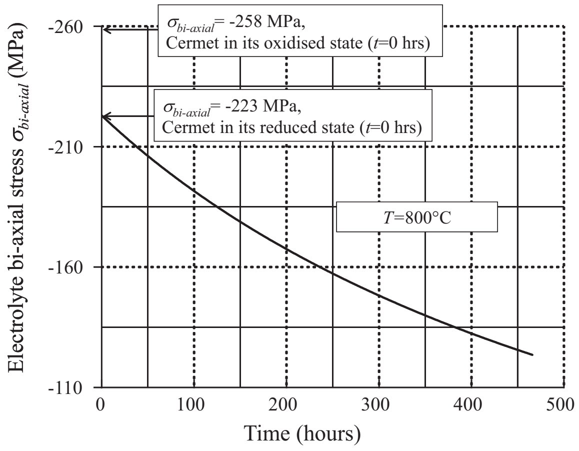

Fig. 11. Simulated electrolyte bi-axial stress at 800 °C (i) after manufacturing, (ii) after the cermet reduction and (iii) plotted as a function of time in operation at 800 °C under hydrogen. The stress has been taken in the middle of the electrolyte.

met "redox" cycles induces a large compressive loading of this layer. An experimental study[8] has been carried out on the effect of these "redox' cycles. It has been shown that a large irreversible deformation of the cermet layer arises as soon as the cermet is subjected to a few number of "redox" cycles. It has been proposed that this phenomenon could be ascribed to a stress relaxation caused by the material plastic strain. Although the microstructure of a thin cermet layer is rather different of the studied thick substrate, these experimental observations can be reasonably considered to be consistent with the cermet creep properties measured in this work.

6. Conclusion

A methodology has been proposed in this study to investigate the creep properties of porous Ni-8YSZ cermet. The creep experiments have been conducted under reducing atmosphere at the SOFC operating temperature. Specimens have been loaded in a four-point bending test bench. The level of stress has been chosen in such way that it is representative for SOFC application. The creep parameters have been identified according to the experimental results in the frame of an analytical and numerical formulation of the mechanical test.

It has been highlighted that Ni-8YSZ exhibits substantial creep strain rates even at relative low temperatures. The creep exponent has been found to be just slightly higher than unity ($1 < n < 2$) suggesting that the creep mechanism has to be ascribed to a diffusional process.

The deformation of both phases of the composite has been estimated through the local stress acting on the cermet particles. This analysis has shown that the metallic phase does not limit the deformation of the cermet which seems to be rather controlled by the creep strain of the 8YSZ network. The cermet creep activation energy has been determined to $Q = 115\,\text{kJ mol}^{-1}$. This value is lower than the ones corresponding to the volume or grain boundary diffusion of Zr^{4+} cations in 8YSZ material. An explanation might be that cermet creep is controlled by the cations diffusion in surface rather than in the bulk of the 8YSZ material.

Internal stresses in SOFC have been simulated in operation considering the usual ASC design. It has been shown that cermet creep strain can induce a substantial stress decrease in the thin electrolyte: the compressive stress which tends to protect this layer is predicted to be divided by a factor two after only ~500 h of operation at $T = 800\,^\circ\text{C}$.

Acknowledgements

The authors would like to thank Drs. F. Lefebvre-Joud and M. Reytier for many useful discussions and the critical reading of the manuscript. This work has been obtained in the framework of a national research program called OXYGENE, led by S. Hody from GdF/Suez and financed by the French National Research Agency ANR agency (contract number ANR-08-PANH-012-02).

Appendix A. Modelling of the bending creep test

A.1. General assumption

Hollenberg et al.[22] have initially proposed an analytical modelling of the bending creep test considering the plane stress condition. This work has been generalised here to the plane strain condition. It is assumed that compression creep is symmetrical with respect to tension creep. This hypothesis means that the neutral axis remains in coincidence with the central axis of the beam.[24] The reliability of this assumption has been checked for a porous plasma-sprayed YSZ material[20]: at low stresses and temperatures (800–1000 °C), the authors have recorded no significant displacement of the neutral axis. This result can be reasonably extended to the Ni-YSZ cermet behaviour since its creep deformation is controlled by the YSZ phase.

The viscous plastic strain rate $d\varepsilon_{ij}^{pl}/dt$ is expressed as a function of the plastic potential Ω as follows:

$$\frac{d\varepsilon_{ij}^{pl}}{dt} = \frac{\partial \Omega}{\partial \sigma_{ij}} \tag{A1}$$

The generalisation to the power law model for a 3D representation is done by using the Von Mises criterion. The potential Ω is then expressed as a function of the Von Mises equivalent stress $\sigma_{VM} = \sqrt{3/2 s_{ij} s_{ij}}$ (where s_{ij} denotes the deviatoric part of the stress tensor) [26]:

$$\Omega = \frac{A}{n+1}\left\{\frac{\sigma_{VM}}{A}\right\}^{n+1} \tag{A2}$$

By introducing Eq. (A2) into (A1), the plastic strain rate is also given by:

$$\frac{d\varepsilon_{ij}^{pl}}{dt} = A(\sigma_{VM})^n \frac{\partial \sigma_{VM}}{\partial \sigma_{ij}} \tag{A3}$$

It can be noticed that $(\partial\sigma_{VM}/\partial s_{ij}) = (3/(4\sigma_{VM})) \times (\partial(s_{ij}s_{ij})/\partial s_{ij}) = (3/2)(s_{ij}/\sigma_{VM})$ and $(\partial s_{ij}/\partial\sigma_{ij}) = 1$. Eq. (A3) can then be written as follows:

$$\frac{d\varepsilon_{ij}^{pl}}{dt} = \frac{3}{2}A(\sigma_{VM})^{n-1}s_{ij} \tag{A4}$$

It is assumed the existence of a steady-state creep (involving that stresses are time independent). This hypothesis means that the elastic strain rates $d\varepsilon_{ij}^{elas}/dt$ are equal to zero. Therefore, the total strain rates $d\varepsilon_{ij}^{tot}/dt$ correspond to the plastic ones:

$$\frac{d\varepsilon_{ij}^{tot}}{dt} = \frac{3}{2}A(\sigma_{VM})^{n-1}s_{ij} \tag{A5}$$

A.2. Stresses calculation

A.2.1. Determination of σ_z in plane strain condition

The system of coordinates considered for the present analysis is described in Fig. 1. In plane stress assumption, σ_z is equal to zero. In plane strain condition, the elastics deformation ε_z^{elas} is transformed into a plastic one, meaning that:

$$\frac{d\varepsilon_z^{pl}}{dt} = -\frac{d\varepsilon_z^{elas}}{dt} \tag{A6}$$

The first term of this equation is given by Eq. (A4) and the second term derived from the Hook's relations (with $\sigma_y = 0$ and $\sigma_x =$ imposed $\Rightarrow d\varepsilon_z^{elas}/dt = (1/E)(d\sigma_z/dt)$):

$$\left(\sigma_z - \frac{\sigma_x}{2}\right) \times (\sigma_x^2 + \sigma_z^2 - \sigma_x\sigma_z)^{(n-1)/2} = -\frac{1}{AE} \times \frac{d\sigma_z}{dt} \tag{A7}$$

In the steady state $(d\sigma_z/dt) = 0$ and according to the previous expression, the out of plane stress component σ_z becomes equal to:

$$\sigma_z = \frac{\sigma_x}{2} \text{ (steady state solution)} \tag{A8}$$

Before reaching this asymptotic value, some transient stress states will occur. They can be determined by solving the differential Eq. (A7).

For instance, for $n = 1$: $\sigma_z(t) = (1/2)\sigma_x + (\upsilon - (1/2)) \times \sigma_x \times \exp(-AEt)$, and for $n = 2$:

$$\sqrt{\frac{4}{3}}\frac{1}{\sigma_x} \times \left[Argsh\left(\left|\sqrt{\frac{3}{4}}\frac{\sigma_x}{(\sigma_z - (\sigma_x/2))}\right|\right) - Argsh\left(\left|\sqrt{\frac{3}{4}}\frac{1}{(\upsilon - (1/2))}\right|\right)\right] = AEt$$

A.2.2. Determination of σ_x

Eqs. (A5) and (A8) can be used to express the longitudinal beam strain ε_x^{tot}:

$$\varepsilon_x^{tot} = J(t) \times (\sigma_x)^n \text{ with } J(t) = \begin{cases} At + \text{constant} & \text{in plane stress} \quad \text{(a)} \\ A\left(\dfrac{3}{4}\right)^{(n+1)/2} t + \text{constant} & \text{in plane strain} \quad \text{(b)} \end{cases} \tag{A9}$$

The term ε_x^{tot} is also linked to the beam curvature $\rho(t)$ according to $\varepsilon_x^{Totale} = (\xi/\rho(t))$ (with $\xi = -y$). The stress can then be expressed as follows:

$$\sigma_x(\xi) = \left(\frac{\xi}{\rho(t) \times J(t)}\right)^{1/n} \tag{A10}$$

The bending moment $M_f = \int_{-h/2}^{+h/2} \xi \times \sigma_x(\xi) \times b\, d\xi$ can be calculated as a function of $J(t)$ and $\rho(t)$:

$$M_f = \frac{I_n}{[\rho(t) \times J(t)]^{1/n}} \text{ with } I_n = 2b \times \frac{n}{n+1} \times \left(\frac{h}{2}\right)^{(2n+1)/n} \tag{A11}$$

where I_n is defined as the "complex" moment of inertia. The stress σ_x is finally given by introducing Eq. (A9) into Eq. (A11):

$$\sigma_x(\xi) = \frac{\xi^{1/n} \times M_f}{I_n} \tag{A12}$$

A.3. Beam deflection

The geometrical relation $1/\rho = (d^2y/dx^2)$ is introduced in Eq. (A12) and leads to the following equation:

$$\frac{d^2y}{dx^2} = J(t) \times \left(\frac{I_n}{M_f}\right)^n \tag{A13}$$

Between the inner bearings (*i.e.* $x \in [(L-a)/2\,;(L+a)/2]$), the bending moment is constant: $M_f = (P \times (L-a)/2)$. Between the outer and inner bearings (*i.e.* $x \in [0\,;(L-a)/2] \cup [(L+a)/2\,;L]$), the bending moment is equal to $M_f = P \times x$. Eq. (A13) can then be integrated by considering the three following boundary conditions:

(i) $y = 0$ for $x = 0$,
(ii) $\frac{dy}{dx} = 0$ for $x = L/2$,
(iii) The slop of the beam must be continuous under the inner bearings: $\left.\frac{dy}{dx}\right)_{x=\left(\frac{L-a}{2}\right)^+} = \left.\frac{dy}{dx}\right)_{x=\left(\frac{L-a}{2}\right)^-}$ for $x = (L-a)/2$.

Finally, the shape of the beam deflection is given by:

$$y(x) = -J(t) \times \left(\frac{P}{I_n}\right)^n \times \Gamma(x) \quad \text{for} \quad x \in \left[\frac{L-a}{2}; \frac{L+a}{2}\right] \tag{A14a}$$

$$y(x) = -J(t) \times \left(\frac{P}{I_n}\right)^n \times \Lambda(x) \text{ for } x \in \left[0; \frac{L-a}{2}\right] \cup \left[\frac{L+a}{2}; L\right] \tag{A14b}$$

with:

$$\Gamma(x) = \left(\frac{L-a}{2}\right)^n \times \left[\left(-\frac{x^2}{2} + \frac{L}{2}x\right) + \frac{L-a}{2} \times \left(\frac{n(a-L)}{4(n+2)}\right)\right] \tag{A15a}$$

$$\Lambda(x) = \left(\frac{L-a}{2}\right)^n \times \left(\frac{a}{2} + \frac{1}{n+1}\frac{L-a}{2}\right) \times x - \frac{x^{n+2}}{(n+1)(n+2)} \tag{A15b}$$

References

1. Singhal SC, Kendall K. In: Singhal SC, Kendall K, editors. *High temperatures solid oxide fuel cells*. Oxford: Elsevier; 2003. p. 17.
2. Suzuki M, Iwata S, Higaki K, Inoue S, Shigehisa T, Shigehisa T, et al. Development and field test results of residential SOFC CHP system. *ECS Trans* 2009;**25**(2):143–7.
3. Föger K. Commercialisation of CFCL's Residential Power Station – Blue-Gen. In: *The 9th European Fuel Cell Forum (Switzerland) Chapter 2*. 2010. p. 22–8.
4. Hody S, Amérigo C. Test of the integrated SOFC micro-CHP boiler developed by De Dietrich Thermique and Ceramic Fuel Cells Ltd. In: *The 9th European Fuel Cell Forum (Switzerland) Chapter 2*. 2010. p. 40–8.
5. Sarantaridis D, Atkinson A. Redox cycling of Ni-based solid oxide fuel cell anodes. *Fuel Cells* 2007;**3**:246–58.
6. Ettler M, Timmermann H, Malzbender J, Weber A, Menzler NH. Durability of Ni anodes during reoxidation cycles. *J Power Sources* 2010;**195**:5452–67.
7. Laurencin J, Delette G, Morel B, Lefebvre-Joud F, Dupeux M. Solid oxide fuel cells damage mechanisms due to Ni-YSZ re-oxidation: case of the anode supported cell. *J Power Sources* 2009;**192**:344–52.
8. Laurencin J, Delette G, Sicardy O, Rosini S, Lefebvre-Joud F. Impact of 'redox' cycles on performances of solid oxide fuel cells: case of the electrolyte supported cells. *J Power Sources* 2010;**195**:2747–53.
9. Laurencin J, Lefebvre-Joud F, Delette G. Impact of cell design and operating conditions on the performances of SOFC fuelled with methane. *J Power Sources* 2008;**177**:355–68.

10. Basu RN, Blass G, Buchkremer HP, Stöver D, Tietz F, Wessel E, et al. Simplified processing of anode-supported thin film planar solid oxide fuel cells. *J Eur Ceram Soc* 2005;**25**:463–71.
11. Fischer W, Malzbender J, Blass G, Steinbrech RW. Residual stresses in planar solid oxide fuel cells. *J Power Sources* 2005;**150**:73–7.
12. Malzbender J, Fischer W, Steinbrech RW. Studies of residual stresses in planar solid oxide fuel cells. *J Power Sources* 2008;**182**:594–8.
13. Laurencin J, Delette G, Lefebvre-Joud F, Dupeux M. A numerical tool to estimate SOFC mechanical degradation: case of the planar cell configuration. *J Eur Ceram Soc* 2008;**28**:1857–69.
14. Morales-Rodríguez A, Bravo-León A, Domínguez-Rodríguez A, López-Esteban S, Moya JS, Jiménez-Melendo M. High-temperature mechanical properties of zirconia/nickel composites. *J Eur Ceram Soc* 2003;**23**:2849–56.
15. Morales-Rodríguez A, Bravo-León A, Domínguez-Rodríguez A, Jiménez-Melendo M. High-temperature plastic behavior of TZP-Ni cermets. *J Am Ceram Soc* 2008;**91**(2):500–7.
16. Gutierrez-Mora F, Ralph JM, Routbort JL. High-temperature mechanical properties of anode-supported bilayers. *Solid State Ionics* 2002;**149**:177–84.
17. Sarantaridis D, Chater RJ, Atkinson A. Changes in physical and mechanical properties of SOFC Ni-YSZ composites caused by redox cycling. *J Electrochem Soc* 2008;**155**(5):B467–72.
18. Zhu D, Miller RA. Sintering and creep behavior of plasma-sprayed zirconia- and hafnia-based thermal barrier coatings. *Surf Coat Technol* 1998;**108/109**:114–20.
19. Zhu, D. and Miller, R. A., Determination of creep behaviour of thermal barrier coatings under laser imposed temperature and stress gradients. *NASA technical memorandum 113169*, ARL-TR-1565.
20. Soltani R, Coyle TW, Mostaghimi J. Creep behavior of plasma-sprayed zirconia thermal barrier coatings. *J Am Ceram Soc* 2007;**90**(9): 2873–8.
21. Ahrens M, Lampenscherf S, Vaßen R, Stöver X. Sintering and creep processes in plasma-sprayed thermal barrier coatings. *J Thermal Spray Technol* 2004;**13**(3):432–42.
22. Hollenberg GW, Terwilliger GR, Gordon RS. Calculation of stresses and strains in four-point bending creep tests. *J Am Ceram Soc* 1971;**54**(4):196–9.
23. Selçuk A, Atkinson A. Strength and toughness of tape-cast yttria stabilized zirconia. *J Am Ceram Soc* 2000;**83**(8):2029–35.
24. Ding JL. Numerical study of time dependent behaviour of GN-10 structural ceramics in bend creep test. *J Mater Sci* 2002;**37**:4165–80.
25. Young WC, Budynas RG. *Roak's Formulas for Stress and Strain*. 7th ed. Mc Graw Hill; 2002. p. 126.
26. Besson J, Cailletaud G, Chaboche JL, Forest S. *Mécanique non linéaire des matériaux*. Hermes; 2001. p. 84.
27. Delette, G. and Giraud, H., *Investigation of the electrolyte robustness.* CEA/DTH report, Real-SOFC EU project, WP 1.5.4.
28. Sun B, Rudkin RA, Atkinson A. Effect of thermal cycling on residual stress and curvature of anode-supported SOFCs. *Fuel Cells* 2009;**9**(6):805–13.
29. Haussonne J-M, Carry C, Bowen P, Barton J. *Céramiques et verres, Principes et techniques d'élaboration*, 16. Presses polytechniques et universitaires romandes; 2005. p. 465.
30. Rice RW. Comparison of stress concentration versus minimum solid area based mechanical property–porosity relations. *J Mater Sci* 1993;**28**:2187–90.
31. Pihlatie MH, Frandsen HL, Kaiser A, Mogensen M. Continuum mechanics simulations of NiO/Ni-YSZ composites during reduction and re-oxidation. *J Power Sources* 2010;**195**:2677–90.
32. Poirier JP. *Plasticité à haute température des solides cristallins*. Eyrolles; 1976. p. 172.
33. Raj R, Ashby MF. On grain boundary sliding and diffusional creep. *Metall Trans* 1971;**2**:1113–27.
34. Frost HJ, Ashby MF. *Deformation Mechanism Maps: The Plasticity and Creep of Metals and Ceramics*. Oxford: Pergamon press; 1982.
35. Kilo M, Borchardt G, Lesage B, Kaïtasov O, Weber S, Scherrer S. Cation transport in yttria stabilized cubic zirconia: ^{96}Zr tracer diffusion in $(Zr_xY_{1-x})O_{2-x/2}$ single crystals with $0.5 \leq x \leq 0.48$. *J Eur Ceram Soc* 2000;**20**:2069–77.
36. Chokshi Atul H. Diffusion, diffusion creep and grain growth characteristics of nanocrystalline and fine-grained monoclinic, tetragonal and cubic zirconia. *Scr Mater* 2003;**48**:791–6.
37. Solmon H, Chaumont J, Dolin C, Monty CY. Zr and O self diffusion in $Zr_{1-x}Y_xO_{2-x/2}$ ($x = 0.17$). *Ceram Trans* 1991;**24**:175–84.
38. Suárez G, Garrido LB, Aglietti EF. Sintering kinetics of 8Y-cubic zirconia: cation diffusion coefficient. *Mater Chem Phys* 2008;**110**:370–5.
39. Cannon WR, Langdon TG. Review, creep of ceramics, part 2: an examination of flow mechanisms. *J Mater Sci* 1988;**23**:1–20.
40. Lakki A, Herzog R, Weller M, Schubert H, Reetz C, Görke O, et al. Mechanical loss, creep, diffusion and ionic conductivity of ZrO_2–8 mol%Y_2O_3 polycrystals. *J Eur Ceram Soc* 2000;**20**:285–96.
41. Withey E, Petorak C, Trice R, Dickinson G, Taylor T. Design of 7 wt.% Y_2O_3–ZrO_2/mullite plasma-sprayed composite coatings for increased creep resistance. *J Eur Ceram Soc* 2007;**27**:4675–83.
42. Thurn G, Schneider GA, Aldinger F. High-temperature deformation of plasma-sprayed ZrO_2 thermal barriers coatings. *Mater Sci Eng* 1997;**A233**:176–82.
43. Erk KA, Deschaseaux C, Trice RW. Grain-boundary grooving of plasma-sprayed yttria-stabilized zirconia thermal barrier coatings. *J Am Ceram Soc* 2006;**89**(5):1673–8.
44. Jiménez-Melendo M, Domínguez-Rodríguez A, Castaing J, Marquez R. Diffusion and creep: application to deformation maps on NiO. *Scr Metall* 1986;**20**:739–42.
45. Nakajo A, Stiller C, Härkegård G, Bolland O. Modeling of thermal stresses and probability of survival of tubular SOFC. *J Power Sources* 2006;**158**:287–94.